Author's personal copy

Journal of Materials Science: Materials in Electronics (2020) 31:14823–14837
https://doi.org/10.1007/s10854-020-04045-8

Surface decoration of $MnWO_4$ nanoparticles with g-C_3N_4 nanosheets to build hetero-structure and its structural, optical and enhanced visible light photocatalytic activity

V. Rathi[1] · A. Panneerselvam[2] · R. Sathiyapriya[3]

Received: 12 February 2020 / Accepted: 18 July 2020 / Published online: 25 July 2020
© Springer Science+Business Media, LLC, part of Springer Nature 2020

Abstract
In this study, we report the synthesis of manganese tungstate ($MnWO_4$)/graphitic carbon nitrides (g-C_3N_4) hybrid photocatalysts by simple hydrothermal method. The prepared photocatalysts have been characterized by X-ray diffraction (XRD), transmission electron microscopy (TEM), energy dispersive X-ray (EDX) analysis, X-ray photoelectron spectroscopy (XPS), Raman spectroscopy, photoluminescence spectroscopy (PL) and UV–visible spectroscopy. XRD and TEM results reveal that the both pure and composite samples have monoclinic wolframite structure with spherical nanoparticles, which is decorated on the surface of g-C_3N_4 sheets. A considerable red shift in the absorption and narrowing the band gap (3.02–2.55 eV) energy was observed in the $MnWO_4$/g-C_3N_4 composite samples. The photocatalytic measurements exhibit that the optimized photocatalyst (15 wt%-$MnWO_4$/g-C_3N_4) show high degradation efficiency (98%) and long-term stability towards rhodamine (RhB) dye under visible light irradiation. The J-V characteristics reveal that $MnWO_4$/g-C_3N_4 photoanode show high photoconversion efficiency (PCE%) of 7.15%, which is higher than that of pure $MnWO_4$ (2.34%). The significant enhancement in the photocatalytic behavior is due to the coactions between the g-C_3N_4 nanosheets and $MnWO_4$ nanoparticles.

1 Introduction

Photocatalysis using semiconductors has become an area of great research interest because of its potential applications in solving energy supply and environmental pollution problems. However, the applications of single-phase photocatalysts are usually restricted by limited visible light responses and the high electron–hole recombination rates, which play essential roles in determining the photocatalytic activity. Heterojunction photocatalysts can incorporate multiple functionalities by integrating different individual materials within the same structure. Moreover, the synergistic effects of heterojunctions can significantly reduce the recombination and speed up the separation rate of photogenerated charge carriers, resulting in an enhancement of photocatalytic activity [1–5]. Thus, heterojunction photocatalysts have become increasingly attractive among all photocatalysts. Generally, semiconductor photocatalysts have attracted wide spread interest as promising materials for the removal of organic contaminants. Nevertheless, the most widely used photocatalysts, TiO_2, suffers from two main problems, which are the low solar energy conversion efficiency and the high recombination of photogenerated electron–hole pairs. Therefore, great efforts have been devoted to searching for new efficient photocatalysts. In the past years, a series of conjugated material (C60, PANI, graphene, g-C_3N_4, etc.) have been demonstrated to improve photocatalytic properties. Among them, g-C_3N_4 is considered as a promising candidate for preparation of hetero-nanostructure photocatalysts [6–10]. It is a soft polymer so that it can easily coat on other compounds surface. On the other hand, its graphene-like sp2 bonding structure, together with abundant in-plane nitrogen dopants and defects, gives it an appealing electronic structure, which is responsible for its multi-functional catalytic activity. Compared with other photocatalysts, g-C_3N_4 combines the advantages of low cost, nontoxicity and visible

✉ A. Panneerselvam
panneer.phy@gmail.com

[1] Department of Physics, Vivekanandha College of Technology for Women, Namakkal, Tamilnadu 637205, India

[2] Department of Physics, Vivekanandha College of Engineering for Women, Tiruchengode, Namakkal, Tamilnadu 637205, India

[3] Department of Physics, Mahendra Engineering College, Namakkal, Tamilnadu 637503, India

Author's personal copy

light activity. Even though, the application of pure g-C_3N_4 is limited by small surface area, rapid recombination of the photogenerated e^-/h^+ pair and low quantum efficiency [11–16]. Different strategies have been investigated to promote the photocatalytic activity of g-C_3N_4 including doping with metal and non-metal particles [17, 18], combination with other semiconductors [19, 20], polymers [21], carbon nanomaterials [22–24]. Generally, combination of g-C_3N_4 with metal oxides is the effective way to enhancing the photocatalytic efficiency. This is due to a better separation of the photo-induced electron–hole pairs and longer lifetime of the photo-generated charge carriers of the bulk *g*-C_3N_4. Recently, a large number of metal oxides combination with g-C_3N_4 heterojunction catalysts such as WO_3/g-C_3N_4 [25], CdS/g-C_3N_4 [26], NiO/g-C_3N_4 [27] and Fe_2O_3/g-C_3N_4 [28] have been effectively investigated their photocatalytic properties. Currently metal tungstate based oxide nanomaterials has broadly studied as the catalyst materials, which has been used in the different types of applications such as electro-chromic windows, photocatalyst, bio sensors and gas sensors. Manganese tungstate ($MnWO_4$) is the most probable binary metal oxides with suitable band gap ($E_g = 2.7$ eV) with tunable optical and electrical properties which is combination with g-C_3N_4. For example, Hassan et al. synthesized $MnWO_4/TiO_2$ composite catalyst and studied the methyl orange degradation performance under visible light [29]. Saranya et al. [30] have reported electrical and electrochemical properties of $MnWO_4$ nanorods ultrasonic method. The conductivity of $MnWO_4$ prepared through surfactant-assisted ultrasonication method was 4.23×10^{-5} S/cm and through ultrasonication method was 1.186×10^{-6} S/cm at 570 °C. Aloysius Sabu et al. [31] reported electronic properties such as dielectric constant, loss and AC conductivity of $MnWO_4$ nanoparticles synthesized by simple chemical precipitation method. The results reveal that the Ac conductivity value of σac for $MnWO_4$ is 0.48×10^{-5} S/m at 100 Hz, while the value is are 3.45×10^{-5} S/m at 10 MHz. CdS/$MnWO_4$ [32] and $MnWO_4$/BiOI [33] nanocomposites was also utilized to visible light induced photodegradation performance of various dyes. The results exhibits that high degradation performance of $MnWO_4$/g-C_3N_4 composite such as high efficiency, kinetics rate and high stability was achieved towards methylene blue and rhodamine B dyes than compared with bare $MnWO_4$ catalyst. Inspired these publications and as a part of our ongoing research work on tungsten based photocatalysts, we report herein investigation on the photocatalytic activity of $MnWO_4$/g-C_3N_4 hybrid photocatalysts for the degradation of induced rhodamine B (RhB) and 4-chlorophenol (4-CP) dyes in a suspension system. To the best of our awareness the high performance photocatalytic properties of $MnWO_4$/g-C_3N_4 hybrid catalyst was not reported previously.

2 Experimental procedure

2.1 Materials

Melamine ($C_3H_6N_6$, 99%) was used as a carbon nitride precursor. Manganese sulfate ($MnSO_4 \cdot H_2O$), sodium tungstate ($Na_2WO_4 \cdot 2H_2O$), rhodamine B (RhB) and 4-chlorophenol (4-CP) solutions were purchased from Alfa Aesar, Japan (purity of 99%). These chemicals were used as received without any further purification.

2.2 Preparation of g-C_3N_4, $MnWO_4$ and $MnWO_4$/g-C_3N_4 nanocomposites

Bare g-C_3N_4 was synthesized from Melamine, which is direct annealing of 400 °C for 2 h in air environment [34]. A facile hydrothermal route was used to prepare the $MnWO_4$ nanoparticles. Initially, 1 g (0.5 mol) of $MnSO_4 \cdot H_2O$ and 2 g (0.5 mol) of $Na_2WO_4 \cdot 2H_2O$ were dissolved in 50 ml of DI water using 100 ml beaker. The solution was stirred vigorously to attain the clear homogenous mixture. Then the resultant sol was placed to Teflon-lined autoclave, which is maintained as 120 °C for 24 h. After the hydrothermal reaction the product was washed and centrifuged with ethanol and DI water to remove the excess contaminant and finally dried at 80 °C for hot air oven. The $MnWO_4$/g-C_3N_4 photocatalysts were prepared through several steps. First, an appropriate amount of g-C_3N_4 was added into methanol to be ultrasonically stirred for 1 h to completely disperse the g-C_3N_4. After $MnWO_4$ powder was added, the solution was stirred in the fume hood for 24 h. Finally the mixture was dried at 100 °C overnight and then heated to 300 °C for 2 h. The $MnWO_4$/g-C_3N_4 composites had different ratios of g-C_3N_4 to $MnWO_4$. The mass ratios (weight%) of the resulting samples were as follows: g-C_3N_4:$MnWO_4$ = 1:1, 2:1, and 3:1. The samples with different ratio were named as MWG1, MWG2 and MWG3, respectively.

2.3 Characterization techniques

Bruker D8 diffractometer with Cu Kα radiation ($\lambda = 1.5418$ Å) was used to analysis the structural nature of the samples. The microstructure and elemental composition of the samples were analyzed by using scanning electron microscope (JEOL Model JSM—6390LV), transmission electron microscope (TEM, H-600-II, Hitachi) and energy dispersive spectra (EDS) (JEOL Model JED—2300) analysis. The fundamental vibration modes of the samples were measured by Fourier transforms infrared spectroscopy (FT-IR, Nicolet Nexus 470). The specific surface areas and porous nature of materials were further investigated by nitrogen adsorption/desorption measurements

Author's personal copy

on nova 2200e. BRUKER RFS 27: spectrometer and Perkin-Elmer lambda 950 UV–Vis.–NIR spectrophotometer was utilized to identify the vibration mode and optical nature of the photocatalysts.

2.4 Photocatalytic assembly

A glass-type photo-reactor consists of 500 ml capacity with dimension of 15 cm diameter and 20 cm height. Xenon lamp XQ-500 W with an intensity of 40 mW/cm^2 has been used as the source of visible light to activate the photocatalytic reaction. Initial concentration of the solution consists of 10 mg of catalyst powders with mixed with 50 ml of dyes (20 mg/l) and stirred for about 30 min to attain the adsorption–desorption equilibrium. The absorption ability of rhodamine B (RhB) and 4-chlorophenol (4-CP) dyes was monitored using UV–Vis–NIR spectrophotometer (UV-2600SHIMADZU) with the corresponding wavelength of 540 and 220 nm, respectively. The visible light activation time is varied from 0 to 100 min with optimum interval of 20 min the degradation efficiency and first-order kinetics was calculated from previous works [35, 36].

3 Results and discussion

3.1 Powder X-ray diffraction (XRD) analysis

The crystallographic information of the photocatalysts was studied through powder XRD and the corresponding diffraction pattern is shown in Fig. 1. There are two prominent diffraction g-C_3N_4-related peaks at $2\theta = 13.2°$ and 27.4° that correspond to (100) and (002) orientation of interplanar graphitic structural packing [37]. The pristine $MnWO_4$ catalyst shows monoclinic wolframite structure with the space group P2/c, which can be identified by the following miller indices such as (100), (011), (111), (002), (111), (111), (002), (102) (121), (221) and (113), respectively (JCPDS No. 800134). The absence of impurity peaks in the pattern indicates that purity of the products. All the composite samples consist with both g-C_3N_4 and $MnWO_4$ planes, which prove that successful exfoliation of $MnWO_4$ on the g-C_3N_4 matrix. Moreover, the intensity of the peaks becomes highly intense than bare $MnWO_4$. This could be due to the improved behavior of crystalline nature, which is also confirmed by the estimated crystalline sizes.

The average crystallite size can be determined through Debye–Scherer's equation as follows [38]:

$$d = \frac{K\lambda}{\beta \cos\theta},$$

where d is the mean crystallite size, K is the shape factor taken as 0.89, λ is the wavelength of the incident beam, β is the full width at half-maximum and θ is the Bragg angle. The average grain size was calculated to be 22, 26, 31, 36 42 nm for g-C_3N_4, $MnWO_4$, MWG1, MWG2 and MWG3, respectively.

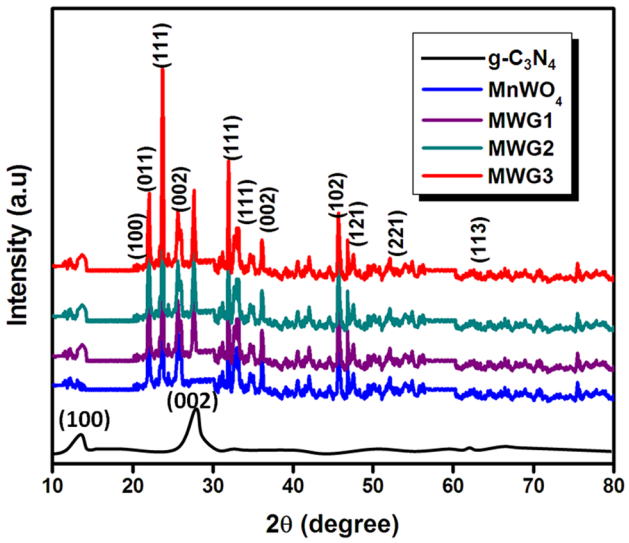


Fig. 1 Powder X-ray diffraction pattern of pure g-C_3N_4, $MnWO_4$ and various composite samples

3.2 Morphological analysis

The morphological and elemental composition of the samples was further analyzed by using SEM, TEM and EDAX images. Figure 2a, b shows SEM images of bare g-C_3N_4 and $MnWO_4$ samples, which consist of sheet-like and spherical shaped morphologies. The clear wrinkle-type nanosheets with lamellar structure and aggregated spherical nanoparticles were identified through the TEM images (Fig. 2c, e). The particle sizes were in the range of 25–35 nm for pristine $MnWO_4$ sample. Further, the $MnWO_4$ nanoparticles were wrapped on the surface of g-C_3N_4 nanosheets. The clear lattice fringes in the lattice have a spacing value of 0.29 nm, equivalent to the (111) plane of monoclinic wolframite structure $MnWO_4$ (inset). The corresponding EDS image of the composite sample comprises Mn, W, O and Cu elements (Fig. 2f). The presence of Cu element is due to the Cu grid. Dynamic light scattering (DLS) (Malvern Instruments Zeta Sizer HPPS) has been used to calculate the particle size of the samples and the relevant graph is shown in Fig. 2g). In this method, light intensity was changed due to the interaction of the particles. The particle sizes are in the range of 30 and 35 nm for $MnWO_4$ and MWG3 samples, which is good accordance with the particles size calculated from the TEM results.

Author's personal copy

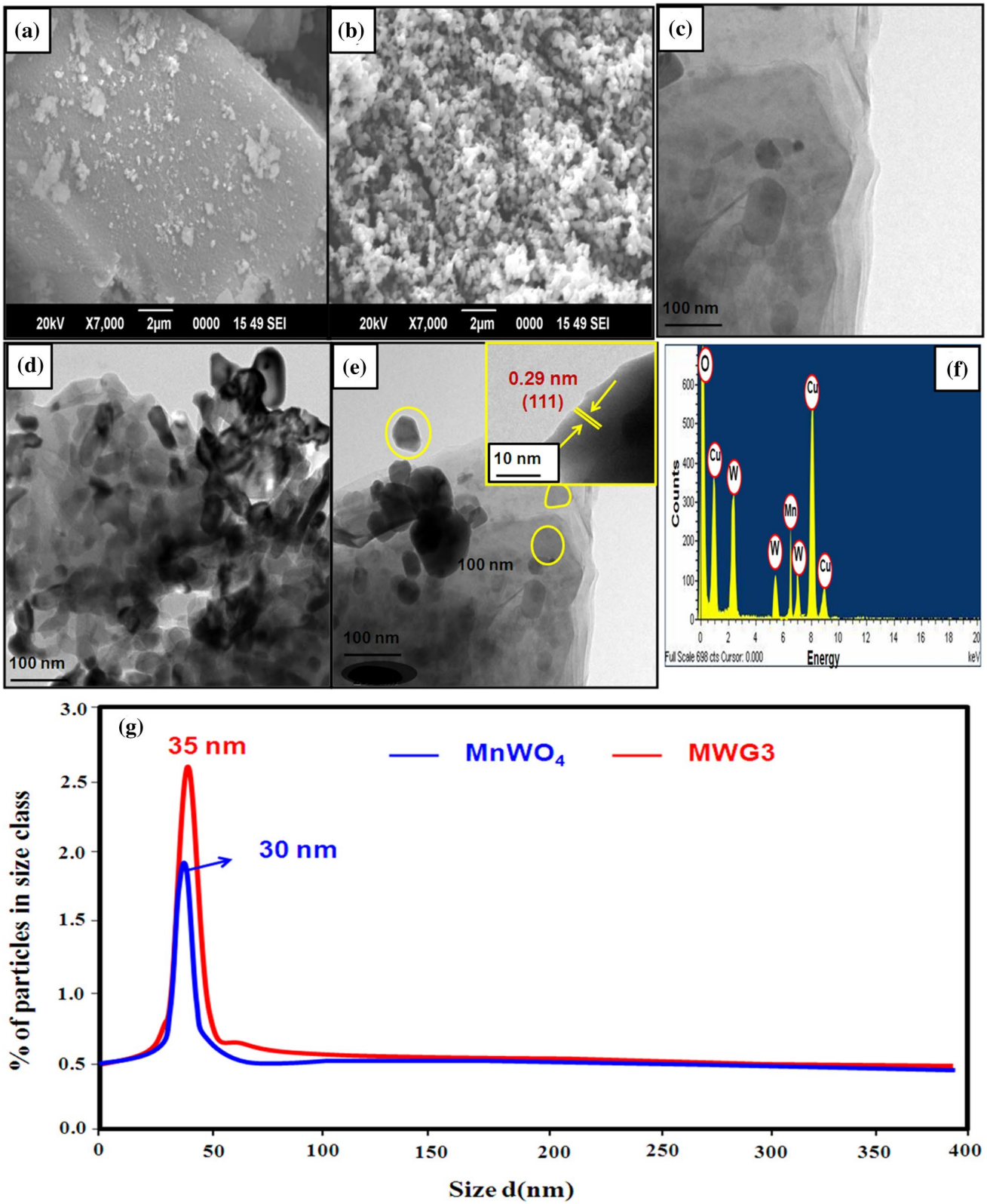


Fig. 2 SEM images of **a** g-C_3N_4; **b** $MnWO_4$; TEM images of **c** g-C_3N_4; **d** $MnWO_4$; **e** MWG3 and **f** EDAX spectra of MWG3 and **g** size distribution of $MnWO_4$ and WMG3 samples, respectively

Author's personal copy

3.3 Raman spectra analysis

A Raman spectrum is a basic technique to differentiate the fundamental vibration modes of carbonaceous and its metal oxide composites. Figure 3 shows the Raman spectra of g-C_3N_4, $MnWO_4$ and its composites. The well-known D and G bands of bare g-C_3N_4 are located at the corresponding of 1342 and 1596 cm^{-1}, respectively [28]. The vibration bands of bare $MnWO_4$ are positioned at 885 and 776 cm^{-1}, is related to symmetric and asymmetric stretching mode of W–O bond, this is perfectly matched well with the already reported values [39]. Combination of both g-C_3N_4 and $MnWO_4$ bands in the composite sample denotes that incorporation of $MnWO_4$ into the g-C_3N_4. Moreover, slight shift was noticed in the lower wave number region for the composite sample. This could be due to the size variation-related defect, which is already confirmed through XRD and TEM results.

3.4 UV–Vis DRS analysis

Figure 4a shows the optical absorption spectra of the catalysts samples. The optical absorption edge was clearly noticed in the visible light region (400–440 nm) for bare g-C_3N_4 and $MnWO_4$ samples, respectively. A considerable red shift in the absorption edge was found after incorporation of g-C_3N_4 into $MnWO_4$. A red shift in the composite sample is due to the increasing the crystalline size or narrowing the optical band gap energy of the samples. In order to further confirm the band gap (E_g), we have using Kubelka–Munk (K–M) model is described below. The K–M model at any wavelength is given by $F(R_\alpha) = (1-R)^2/2R$, where R is the percentage of reflectance. A graph is plotted between $[F(R_\alpha)\, h\upsilon]^2$ vs $h\upsilon$ and the intercept value is the indirect direct band gap energy. Based on the optical absorption the calculated band gap energies are 3.02, 2.88, 2.75, 2.61 and 2.55 eV for bare g-C_3N_4, $MnWO_4$, MWG1, MWG2 and MWG3 samples (Fig. 4b), respectively.

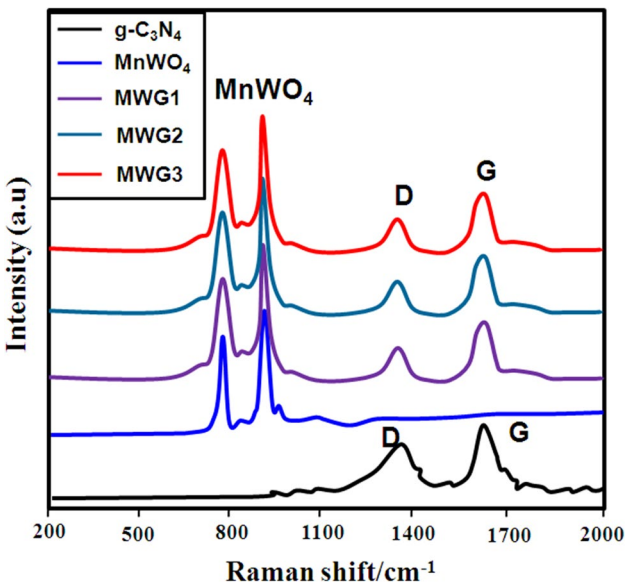


Fig. 3 Raman spectra of pure g-C_3N_4, $MnWO_4$ and various composite samples

3.5 Photoluminescence spectra analysis

Charge separation efficiency of the photocatalysts was analyzed through photoluminescence spectroscopy technique, which gives further information about the structural defects of the samples. Figure 4c shows the room temperature PL spectra of all the catalyst samples which are triggering by He–Ne laser with excitation wavelength ($\lambda_{max} = 320$ nm) as light source. A sharp intense emissions (410, 448 nm) and broad emission (495) was noticed in the all visible to blue green emissions. The intensity of PL emission is significantly reduced in the composite samples than compared with pure catalysts. The decrease in emission peak intensity for $MnWO_4$/g-C_3N_4 composites is due to inhibited recombination of photogenerated electron–hole pairs in g-C_3N_4 and $MnWO_4$ heterojunction, which further indicates a successful charge separation. Time-resolved photoluminescence (TRPL) decay measurements were performed to further evaluate the charge transfer at the $MnWO_4$/g-C_3N_4. Te result is shown Fig. 4d. The normalized TRPL decay shows that $MnWO_4$/g-C_3N_4 samples exhibit faster quenching relative to the bare $MnWO_4$.

3.6 Nitrogen adsorption and desorption analysis

Textural properties, like surface area, pore size distribution and pore volume of the photocatalysts were measured using Nitrogen adsorption and desorption analysis. Figure 5a shows the N_2 adsorption–desorption curve of $MnWO_4$ and MWG3 samples, which is belongs to type II isotherm with H3 hysteresis loop. According to the IUPAC classification both samples resembles to the mesoporous nature [40]. The BET surface area and BJH pore size was found to be 78 m^2/g and 23.54 nm for MWG3 catalyst (Fig. 5b), which is higher than that of bare $MnWO_4$ (43 m^2/g and 37.23 nm). The high surface area and specific porous nature of the composite catalyst would be favorable to improve the photocatalytic activity.

3.7 XPS analysis

Chemical composition and valance state of the MWG3 catalyst were analyzed by XPS and the relevant survey graph is shown in Fig. 5. The wide range XPS graph exposed to Mn 2p, W 4f, O 1s, C 1s, and N 1s (Fig. 5c). In Mn 2p,

Author's personal copy

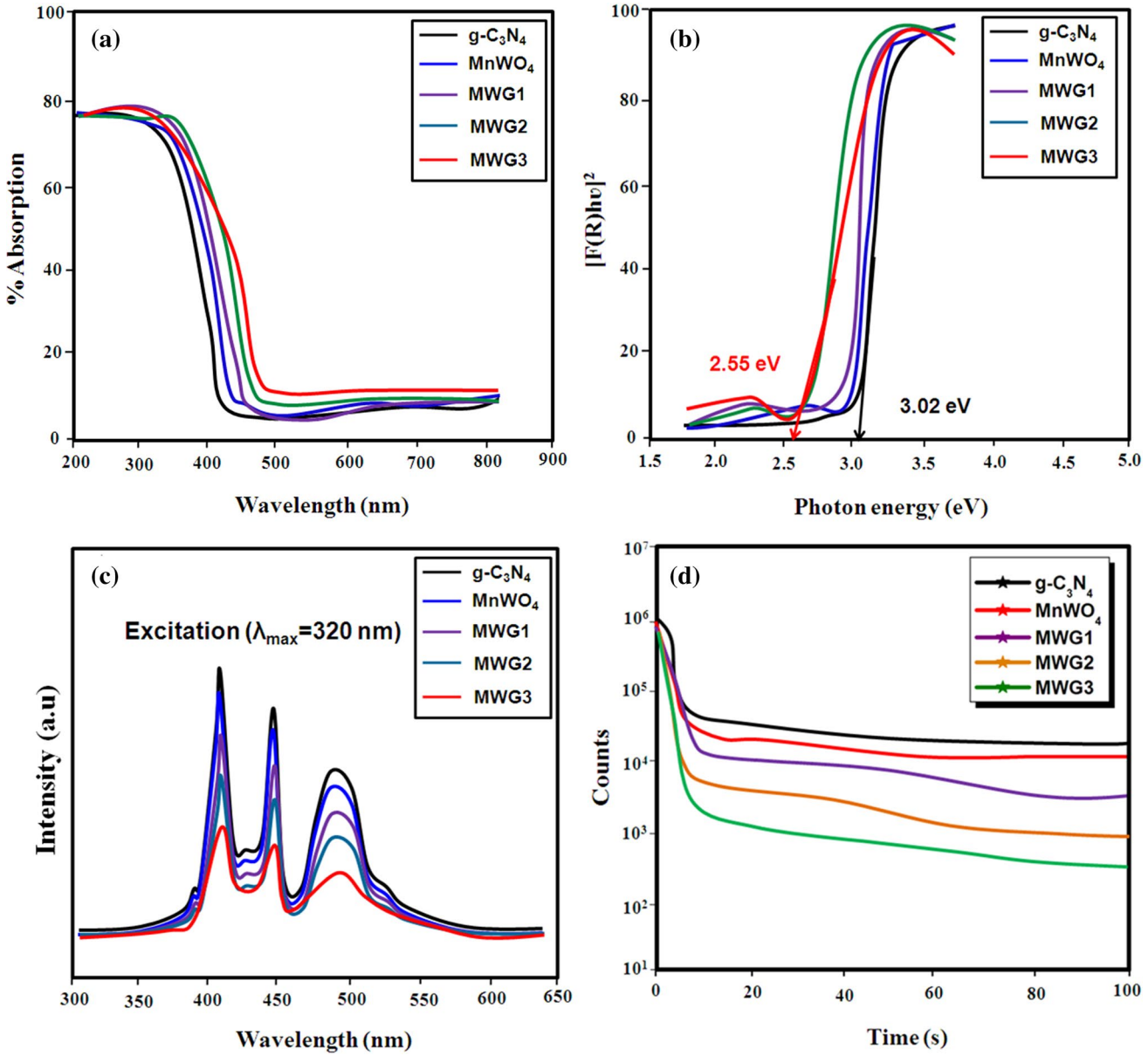


Fig. 4 UV–Vis DRS spectra of pure g-C_3N_4, $MnWO_4$ and various composite catalysts. **a** Absorption spectra, **b** Kubelka–Munk model; **c** photoluminescence spectra of pure g-C_3N_4, $MnWO_4$ and various composite samples; **d** time-resolved PL (TRPL) decays

there are two peaks are observed that corresponds to Mn $2p_{3/2}$ and Mn $2p_{1/2}$ at 640.5 eV and 658.0 eV, respectively (Fig. 5d). It reveals that Mn present in the sample is in +2 oxidation state [41]. A magnification spectrum of W 4f is shown in Fig. 5e. It has two peaks which correspond to W $4f_{7/2}$ and W $4f_{5/2}$ at 34.5 and 37.2 eV, respectively. The W $4f_{7/2}$ and W $4f_{5/2}$ spin–orbit doublets was observed to be 2.2 eV, which can be assigned to the oxidation state of W as +6 [42]. The O 1s peak of is observed at 530.5 eV and 531.8 eV, which might be due to the oxygen species in the metal oxide (Fig. 5f). In the C 1s spectrum (Fig. 5g), the peaks at 282.5 and 286.8 eV belong to the sp^2-C and sp^3-C bonds of g-C_3N_4, respectively. Similarly, the deconvoluted N1s spectrum shows three peaks at 399.5 eV, 400.9 eV, and 402.7 eV (see Fig. 5h), which are assigned to C–N or C≡N, C=N, and N–O bonds, respectively.

3.8 Photocatalytic studies

Initially the absorption ability of the catalyst was evaluated using UV–Vis spectrometer towards RhB and 4-CP dyes under visible light illumination. Figures 6, 7 show the UV–Vis absorption curve of RhB and 4-CP dyes using all the catalysts. The spectrum of visible light source

Author's personal copy

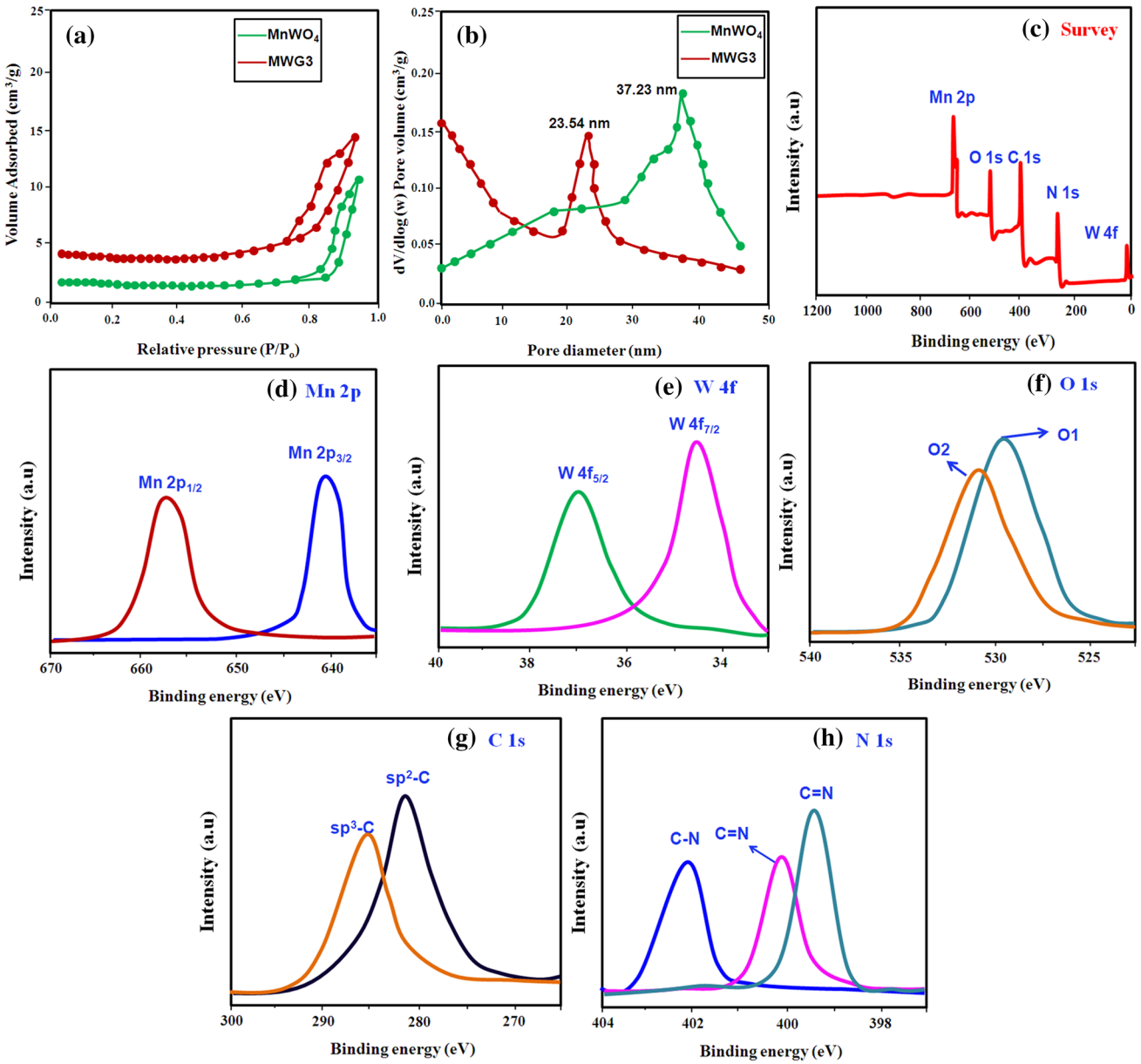
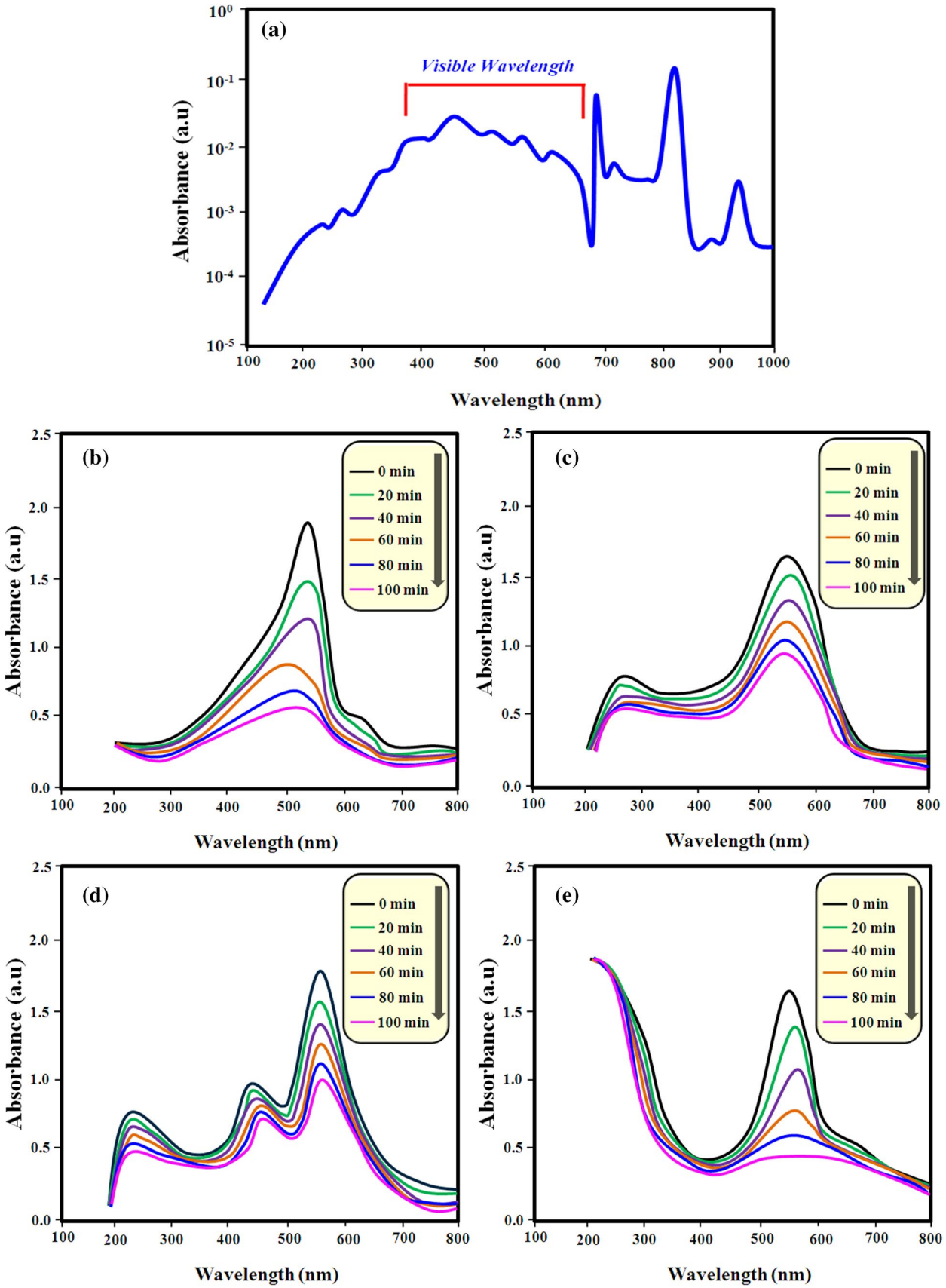


Fig. 5 **a** N_2 adsorption and desorption analysis $MnWO_4$ and MWG3 samples. **b** Corresponding pore size distribution; XPS of MWG3 **c** survey; **d** Mn 2p; **e** W 4f; **f** O 1s; **g** C 1s and **h** N 1s

(xenon lamp XQ-500 W) is shown in Fig. 6a. The maximum absorption wavelength of RhB (540 nm) and 4-CP (220 nm) dyes was gradually diminished with the increase of visible light illumination. In the end of 100 min visible light irradiation the absorption intensity was completely vanish for both dyes. The results suggest that the prepared catalyst were highly photo-active under visible light. Further the degradation efficiency was tested for both dyes under same experimental condition. Figure 8a, b shows the temporal degradation profile of all the catalysts. The bare g-C_3N_4 and $MnWO_4$ catalysts display poor photocatalytic behavior only 32 and 38% of RhB degradation efficiency. After incorporation of $MnWO_4$ into g-C_3N_4 the degradation efficiency was gradually enhanced. After 60 min testing the degradation efficiency of MWG3 catalyst reached 67%, whereas, the maximum degradation efficiency was achieved for 98% at 100 min of visible light irradiation. Among all the catalyst MWG3 showed high photocatalytic performance. The order of the photocatalytic behavior is MWG3 > MWG2 > MWG1 > $MnWO_4$ > g-C_3N_4. The optimum weight ratio (3:1) of the $MnWO_4$/g-C_3N_4 catalyst can noticeable assist the separation of electron–hole pairs leading to improve the photocatalytic efficiency. Similarly, the maximum degradation efficiency of the 4-CP was achieved

Author's personal copy



Author's personal copy

◂**Fig. 6** **a** Spectrum for the visible light source (xenon lamp XQ-500 W); UV absorption spectra of RhB using **b** $MnWO_4$; **c** MWG1; **d** MWG2 and **e** MWG3 catalyst under different illumination time

by MGW3 catalyst (91%) compare than bare $MnWO_4$ (33%). Further the ratio of g-C_3N_4:$MnWO_4$ is adjust to 4:1 and 5:1 and denoted as MWG4 and MWG5, respectively. The degradation efficiency was found to be 50, 78, 98, 91 and 84 for MWG1, MWG2, MWG3, MWG4 and MWG5 catalysts, respectively. The same trend was also obtained in the 4-CP removal efficiency. Hence, the results suggest that the optimum ratio of 3:1 $MnWO_4$/g-C_3N_4 (MWG3) catalyst show superior degradation efficiency compared with other composite catalysts. Based on the previous literature works [43–45] the first-order rate constant was calculated for all the catalysts towards RhB and 4-CP dye solutions (Fig. 8c, d). The results exposed that hydroxyl radicals (OH*) scavenger dominate in the degradation efficiency of both RhB and 4-CP dyes, respectively. In order to understand the charge transfer mechanism leading to RhB and 4-CP mineralization over $MnWO_4$/g-C_3N_4, knowledge of the active species is essential. Radical trapping experiments were carried out to identify the major reactive species responsible for the degradation of the pollutants. Typically, isopropanal (IP), citric acid (CA),

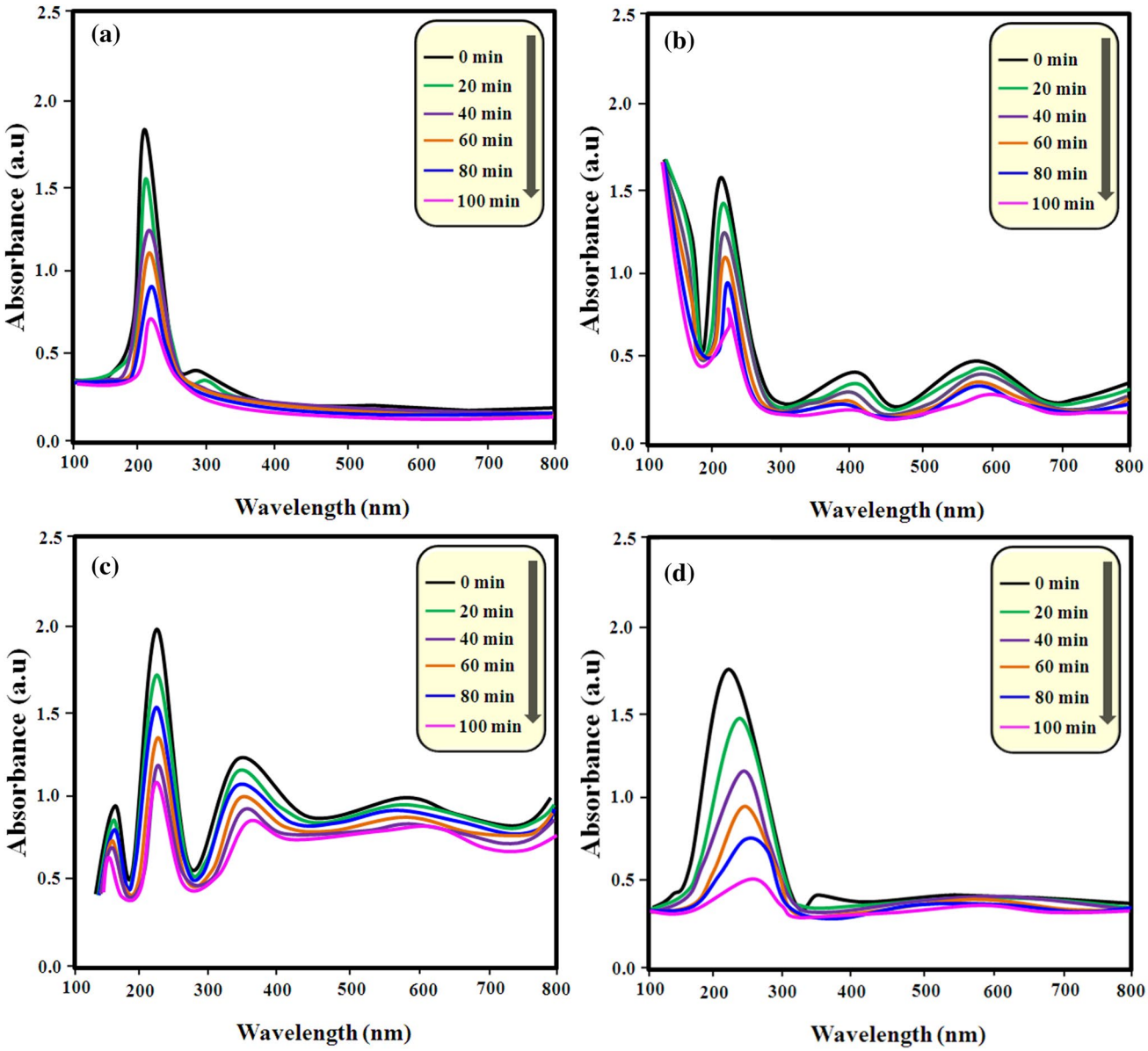
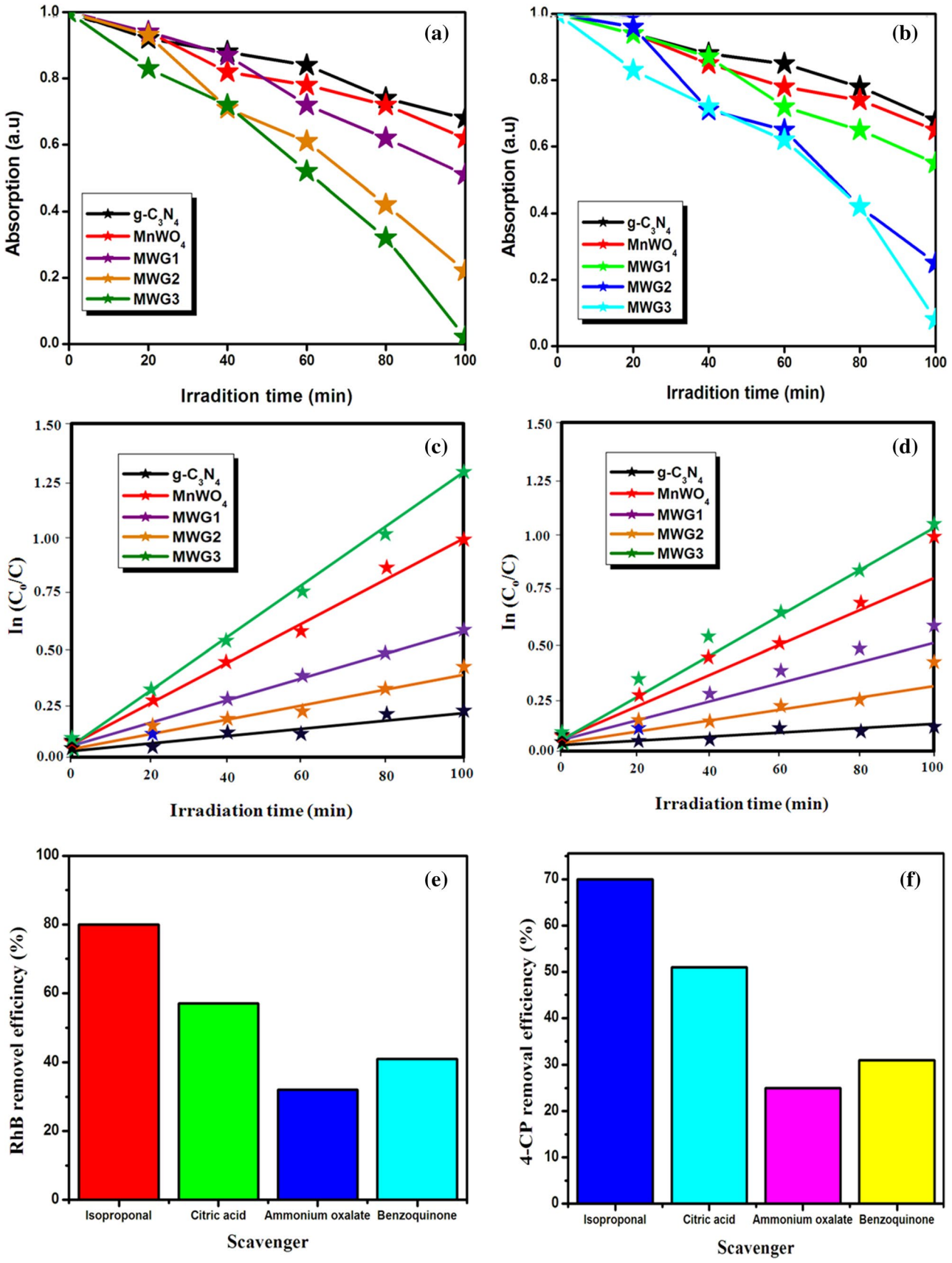


Fig. 7 UV absorption spectra of 4-CP using **a** $MnWO_4$; **b** MWG1; **c** MWG2 and **d** MWG3 catalyst under different illumination time

Author's personal copy



Author's personal copy

◂**Fig. 8** Temporal degradation profile of **a** RhB; **b** 4-CP; Kinetic plot of **c** RhB; **d** 4-CP for all the catalyst powders; Effect of scavenger on the removal efficiency of **e** RhB; **f** 4-CP

ammonium oxalate (AO) and benzoquinone (BQ) were used as scavengers for holes (h^+), hydroxyl radicals ($^*OH$) and superoxide radicals (O_2^{*-}), respectively, and the results are illustrated in Fig. 8e, f. It can be seen that the photocatalytic degradation efficiency of both dyes was significantly suppressed by the addition IP and CA, which indicate that the h^+ and $^*OH$ played a key role in the RhB and 4-CP degradation process. Conversely, only a slight decrease in dye removal was observed after the addition of AO and BQ, suggesting that O_2^{*-} radicals did not play a much significant role. The MWG3 catalyst again proves that high rate constant of RhB is 0.0923 min^{-1}, which is 4 times better than that of bare $MnWO_4$ catalyst (0.0231 min^{-1}). The overall photocatalytic parameters are displayed in Table 1. The COD and TOC mineralizing efficiency was further evaluated in order to prove the high catalytic nature of the obtained catalyst. Figure 9a, b shows the mineralizing efficiency test of RhB and 4-CP pollutants. The results demonstrate that the maximum decolorization efficiency was achieved by MWG3 catalysts, it was found to be 91 and 87% for COD removal efficiency of RhB and 4-CP pollutants. One of the main impacts of the photocatalytic material is long-term stability. The photocatalytic degradation efficiency was further carried out for repeated test (7 cycles) under the same experimental circumstance Fig. 9c, d. After the 7 cycles, a small loss (~2.8%) in the degradation efficiency was found. A slight variation is due to the washing and centrifuge to the catalyst with water and ethanol. The re-usability and long-term stability performance of the obtained catalyst can act as water pollution treatment under visible light illumination. Findings from the photocatalytic results the possible schematic illustration of the photocatalytic mechanism is depicted in Fig. 10. In order to construct a band diagram of the nanocomposite, the energy levels of conduction band (CB) and valance band (VB) of g-C_3N_4 and $MnWO_4$ were calculated using Mulliken electronegativity theory as expressed in Eqs. (1) and (2), respectively,

$$E_{CB} = \chi - E_e + 0.5E_g, \tag{1}$$

$$E_{VB} = E_{CB} - E_g, \tag{2}$$

where E_e is the energy of the free electrons on the hydrogen scale (4.5 eV), χ is the absolute electronegativity of the semiconductor and E_g is the band gap energy of the semiconductor. The calculated valence and conduction band potentials lie at 1.635, − 1.061 eV for g-C_3N_4 and 1.748 and − 0.355 eV, for $MnWO_4$, respectively. These values are consistent with literature reports [46, 47]. Owing to their mild band gaps, both g-C_3N_4 and $MnWO_4$ could be activated by visible light yielding electrons and holes in their conduction bands and valence bands, respectively. Therefore, following excitation, electrons could transfer from the conduction band of g-C_3N_4 (higher potential) to the conduction band of $MnWO_4$ (lower potential) while the holes transfer in the opposite direction and accumulate in the valence band of g-C_3N_4 (Fig. 10). Generally, RhB is not completely activate in the visible light, which is more active under UV light than visible light illumination. In our case, the RhB degradation efficiency is significantly improved by composite sample under visible light illumination. This could be due to the interaction RhB on the catalyst under visible light, which results in rapid release of photo-excited electrons. Under the visible light illumination, g-C_3N_4 could motivate the invention of photogenerated hole pairs at the same time as the electrons on the conduction band can rapidly transfer to the conduction band of $MnWO_4$. Further it can react with the oxygen molecules to generate the O_2 radicals, which stimulate the photocatalytic process under visible light. On the other hand, incorporation of g-C_3N_4 on the $MnWO_4$ would decrease the bandgap with high absorption ability in the visible light region and suppression the process of electron–hole pairs recombination are the factors to improve the photocatalytic efficiency, which is consistent with UV and PL results. Hence, the new type of hybrid catalyst is preferable for degradation of other organic and inorganic dyes under visible light.

3.9 Photovoltaic studies

A 500-W xenon optical filter is used as a solar stimulator to execute the photovoltaic performance of the device. The experiment was done in ambient atmosphere using an experimental setup and the schematic sketch of the DSSCs device is shown in Fig. 11a. J-V characteristics of bare g-C_3N_4, $MnWO_4$ and its composite-based DSSCs were investigated and results are displayed in Fig. 11b and the related photovoltaic parameters are summarized in Table 2. It can be seen that the device based on bare $MnWO_4$ featured a short-circuit current (Jsc) of 6.11 mA/cm^2, an open-circuit voltage (Voc) of 0.43 V and an overall photo-conversion efficiency of 2.34%. Remarkably, the decoration of g-C_3N_4 layer over $MnWO_4$ considerably enhances the device performance. As listed in Table 2, after the incorporation of g-C_3N_4, the Jsc, Voc and η were increased to 13.2 mA/cm^2, 0.721 V and 7.15%, respectively, which was 3.02% increment in comparison to the bare $MnWO_4$ device. What is more, the reason for considerable development of Jsc can be proof by the IPCE (incident photo-to-current conversion efficiency). As displayed in Fig. 11, the device based on $MnWO_4$ decorated with

Author's personal copy

Table 1 Photocatalytic parameters of pure g-C_3N_4, $MnWO_4$ and various composite samples

Samples	Band gap (eV)	Rate constant of RhB		Rate constant of 4-CP		Degradation efficiency at 100 min	
		K (h^{-1})	R^2	K (h^{-1})	R^2	RhB	4-CP
g-C_3N_4	3.17	0.0063	0.965	0.0021	0.921	32	30
$MnWO_4$	3.95	0.0063	0.965	0.0021	0.921	38	34
MWG1	3.75	0.0081	0.966	0.0045	0.938	50	52
MWG2	2.54	0.0099	0.972	0.0058	0.947	78	71
MWG3	2.43	0.0192	0.998	0.0101	0.978	98	91

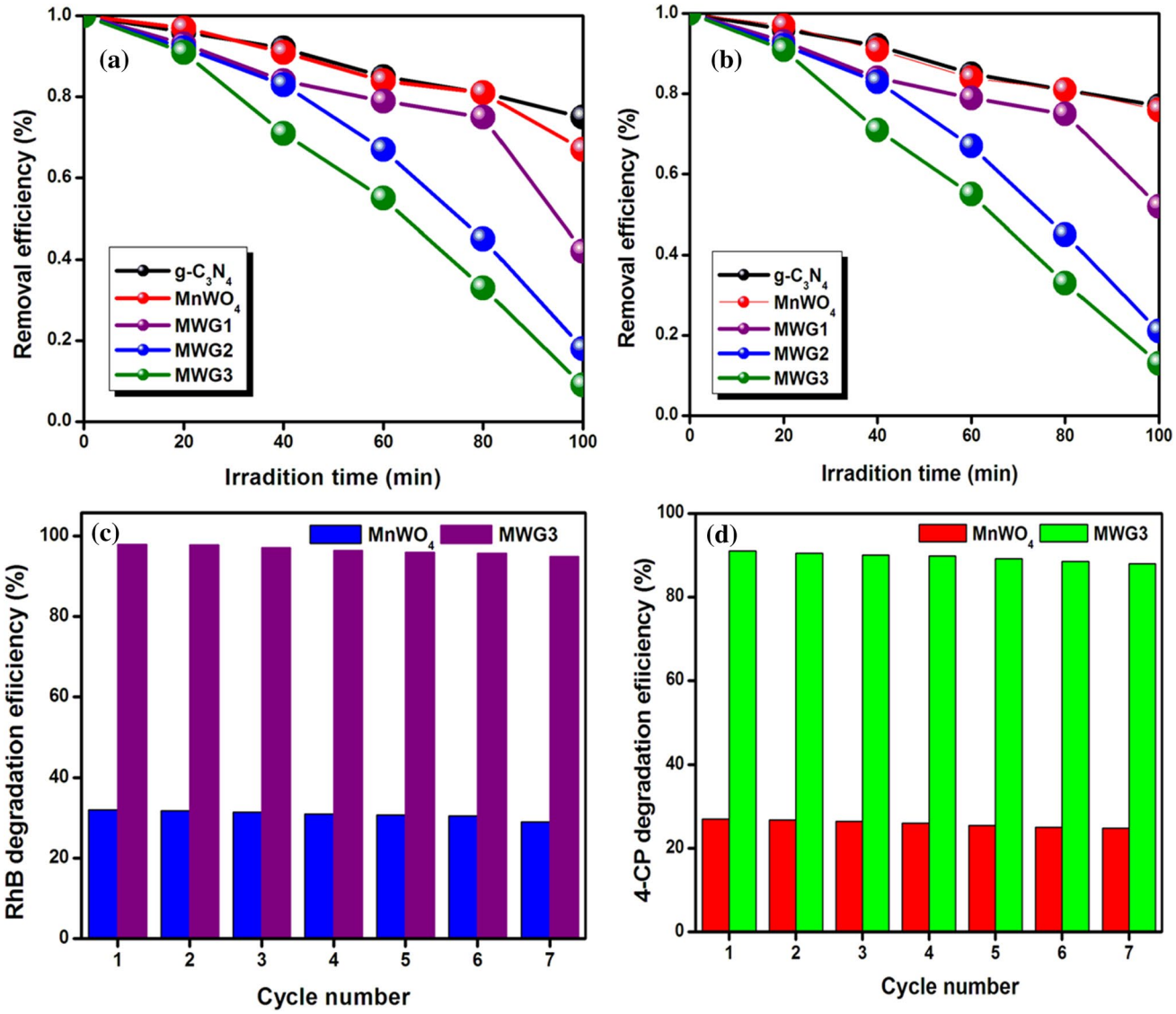


Fig. 9 COD removal efficiency of **a** RhB; **b** 4-CP for all the catalysts; cycling stability test of **c** RhB; **d** 4-CP pollutants using $MnWO_4$ and MWG3 catalyst samples

Author's personal copy

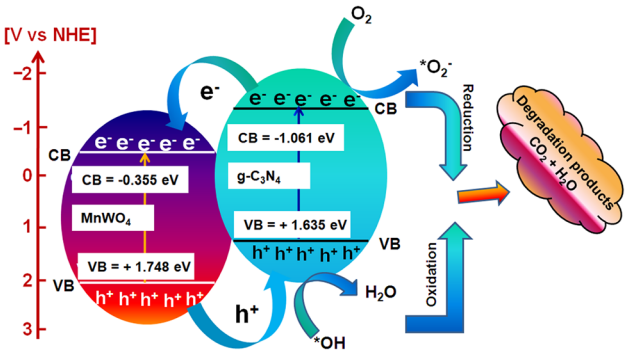


Fig. 10 Schematic representation of the photocatalytic mechanism of the $MnWO_4$/g-C_3N_4 hybrid photocatalyst under visible light irradiation

g-C_3N_4 almost exhibits much higher IPCE in the range of 300 to 800 nm wavelengths than pure ZnO based one. The maximum IPCE was obtained ~ 72.25% at λ ~ 360 nm, in MWG3 photoanode, which is 1.6 times higher than bare $MnWO_4$ photoanode (41.12%) (Fig. 11c).

Table 2 Photovoltaic parameters of pure g-C_3N_4, $MnWO_4$ and various composite samples

Samples	Jsc (mA/cm^2)	Voc (V)	FF (%)	η (%)
g-C_3N_4	5.77	0.46	45.1	1.71
$MnWO_4$	6.11	0.43	48.3	2.34
MWG1	7.02	0.63	52.6	3.45
MWG2	10.87	0.63	58.1	5.51
MWG3	13.21	0.72	72.1	7.15

4 Conclusions

So far, $MnWO_4$/g-C_3N_4 hybrid catalysts were synthesized by facile hydrothermal approach and monitoring the photocatalytic degradation efficiency of RhB and 4-CP dyes under visible light irradiation. The optimized ratio (3:1) of composite sample (MWG3) displayed high photocatalytic activity of RhB such as huge efficiency (98%), high first-order kinetics (is 0.0923 min^{-1}) and long-term stability (loss only 2.8%). This might be attributed to the coactions between the $MnWO_4$ nanoparticles over the surface of

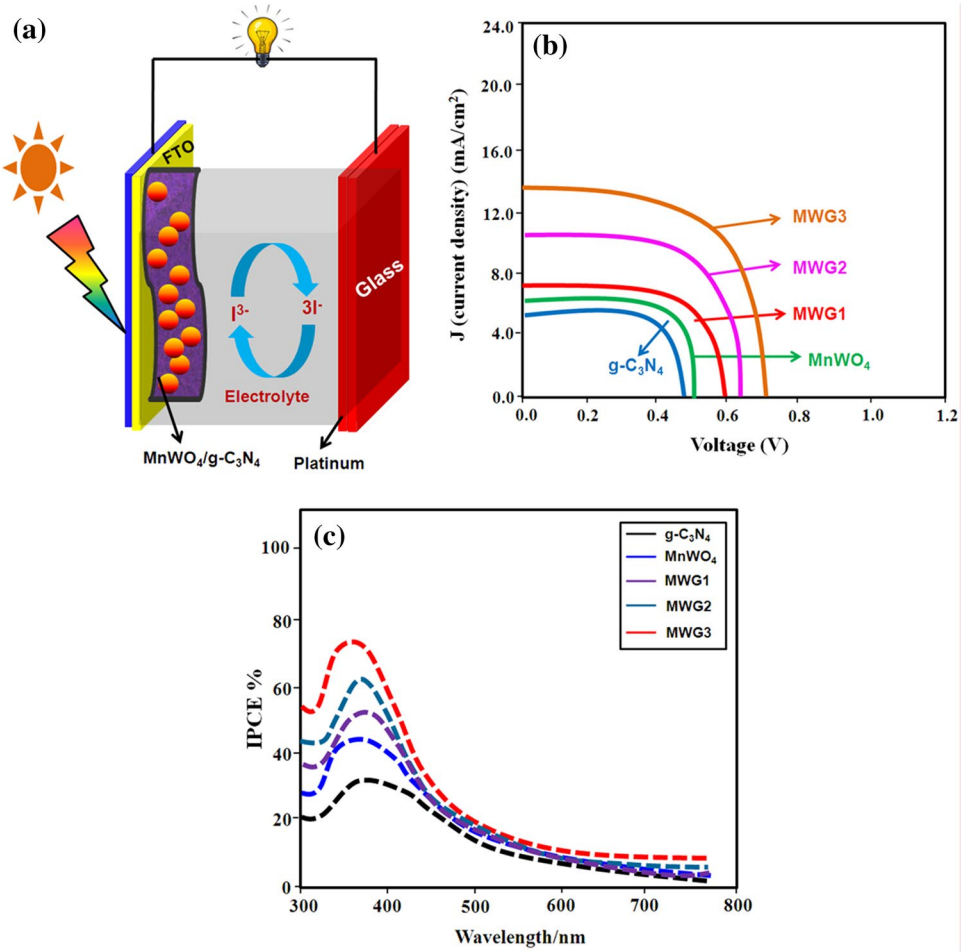


Fig. 11 **a** Schematic sketch of the DSSCs device; **b** J-V characteristics of all the photoelectrodes; **c** IPCE spectra

Author's personal copy

g-C_3N_4 nanosheets. Moreover, slighter reduction in the band gap energy and privileging the reduction to the recombination process of electron–hole pairs are the important factors to enhancing the photocatalytic capability of the composite catalysts. Based on the results, the successive photodegradation of organic dyes in the presence of the hybrid catalysts is possible on sepiolite under visible light to contribute to green chemistry in dye-contaminated water treatment.

References

1. R.S. Blackburn, Natural polysaccharides and their interactions with dye molecules: applications in effluent treatment. Environ. Sci. Technol. **38**, 4905–4909 (2004)
2. J. Ma, W. Song, C. Chen, W. Ma, J. Zhao, Y. Tang, Fenton degradation of organic compounds promoted by dyes under visible irradiation. Environ. Sci. Technol. **39**, 5810–5815 (2005)
3. S. Patnaik, S. Martha, K.M. Parida, An overview of the structural, textural and morphological Modulations of g-C_3N_4 towards photocatalytic hydrogen production. RSC Adv. **6**, 46929–46951 (2016)
4. X. Liu, A. Jin, Y. Jia, T. Xia, C. Deng, M. Zhu, C. Chen, X. Chen, Synergy of adsorption and visible-light photocatalytic degradation of methylene blue by a bifunctional Z-scheme heterojunction of WO_3/g-C_3N_4. Appl. Surf. Sci. **405**, 359–371 (2017)
5. Y. Bao, K. Chen, AgCl/Ag/g-C_3N_4 hybrid composites: preparation, visible light-driven photocatalytic activity and mechanism. Nano-Micro Lett. **8**, 182–192 (2016)
6. J. Fu, Q. Xu, J. Low, C. Jiang, J. Yu, Ultrathin 2D/2D WO_3/g-C_3N_4 step-scheme H_2-production photocatalyst. Appl. Catal. B **243**, 556–565 (2019)
7. J. Wu, N. Li, H.-B. Fang, X. Li, Y.-Z. Zheng, X. Tao, Nitrogen vacancies modified graphitic carbon nitride: scalable and one-step fabrication with efficient visible light-driven hydrogen evolution. Chem. Eng. J. **358**, 20–29 (2019)
8. Y. Yang, C. Zhang, D. Huang, G. Zeng, J. Huang, C. Lai, C. Zhou, W. Wang, H. Guo, W. Xue, R. Deng, M. Cheng, W. Xiong, Boron nitride quantum dots decorated ultrathin porous g-C_3N_4: intensified exciton dissociation and charge transfer for promoting visible-light-driven molecular oxygen activation. Appl. Catal. B **245**, 87–99 (2019)
9. S.A. Ansari, M.H. Cho, Simple and large scale construction of MoS_2-g-C_3N_4 heterostructures using mechano chemistry for high performance electrochemical supercapacitor and visible light photocatalytic applications. Sci. Rep. **7**, 43055 (2017)
10. M. Tahir, C. Cao, N. Mahmood, F.K. Butt, A. Mahmood, F. Idrees, S. Hussain, M. Tanveer, Z. Ali, I. Aslam, Multifunctional g-C_3N_4 nanofibers: a template-free fabrication and enhanced optical, electrochemical, and photocatalyst properties. ACS Appl. Mater. Interfaces **6**, 1258–1265 (2014)
11. L. Liang, L. Shi, F. Wang, L. Yao, Y. Zhang, W. Qi, Synthesis and photo-catalytic activity of porous g-C_3N_4: promotion effect of nitrogen vacancy in H_2 evolution and pollutant degradation reactions. Int. J. Hydrogen Energy **44**, 16315–16326 (2019)
12. L. Shi, F. Wang, J. Sun, The preparation of spherical mesoporous g-C_3N_4 with highly improved photocatalytic performance for H_2 production and rhodamine B degradation. Mater. Res. Bull. **113**, 115–121 (2019)
13. M. Ran, P. Chen, J. Li, C. Wen, J. Li, Y. He, J. Sheng, Y. Sun, F. Dong, Promoted reactants activation and charge separation leading to efficient photocatalytic activity on phosphate/potassium co-functionalized carbon nitride. Chin. Chem. Lett. **30**, 875–880 (2019)
14. H. Li, J. Zhao, Y. Geng, Z. Li, Y. Li, J. Wang, Construction of CoP/B doped g-C_3N_4 nanodots/g-C_3N_4 nanosheets ternary catalysts for enhanced photocatalytic hydrogen production performance. Appl. Surf. Sci. **496**, 143738 (2019)
15. Z. Sun, C. Li, X. Du, S. Zheng, G. Wang, Facile synthesis of two clay minerals supported graphitic carbon nitride composites as highly efficient visible-light driven photocatalysts. J. Colloid Interface Sci. **511**, 268–276 (2018)
16. K. Huang, Y. Hong, X. Yan, C. Huang, J. Chen, M. Chena, W. Shia, C. Liu, Hydrothermal synthesis of g-C_3N_4/$CdWO_4$ nanocomposite and enhanced photocatalytic activity for tetracycline degradation under visible light. Cryst. Eng. Comm. **18**, 6453–6463 (2016)
17. S. Patnaik, D.P. Sahoo, K. Parida, An overview on Ag modified g-C_3N_4 based nanostructured materials for energy and environmental applications. Renew. Sustain. Energy Rev. **82**, 1297–1312 (2018)
18. J. Xu, K.-Z. Long, Y. Wang, B. Xue, Y.-X. Li, Fast and facile preparation of metal doped g-C_3N_4 composites for catalytic synthesis of dimethyl carbonate. Appl. Catal. A **496**, 1–8 (2015)
19. L.-Y. Chen, W.-D. Zhang, In_2O_3/g-C_3N_4 composite photocatalysts with enhanced visible light driven activity. Appl. Surf. Sci. **301**, 428–435 (2014)
20. L. Huang, H. Xu, R. Zhang, X. Cheng, J. Xia, Y. Xu, H. Li, Synthesis and characterization of g-C_3N_4/MoO_3 photocatalyst with improved visible-light photoactivity. Appl. Surf. Sci. **283**, 25–32 (2013)
21. L. Ge, C. Han, J. Liu, In situ synthesis and enhanced visible light photocatalytic activities of novel PANI-g-C_3N_4 composite photocatalysts. J. Mater. Chem. **22**, 11843–11850 (2012)
22. Y. Xu, H. Xu, L. Wang, J. Yan, H. Li, Y. Song, L. Huang, G. Cai, The CNT modified white C_3N_4 composite photocatalyst with enhanced visible-light response photoactivity. Dalton Trans. **42**, 7604–7613 (2013)
23. W.-J. Ong, L.-L. Tan, S.-P. Chai, S.-T. Yong, A.R. Mohamed, Surface charge modification via protonation of graphitic carbon nitride (g-C_3N_4) for electrostatic self-assembly construction of 2D/2D reduced graphene oxide (rGO)/g-C_3N_4 nanostructures toward enhanced photocatalytic reduction of carbondioxide to methane. Nano Energy **13**, 757–770 (2015)
24. J. Xu, H.T. Wu, X. Wang, B. Xue, Y.X. Li, Y. Cao, A new and environmentally benign precursor for the synthesis of mesoporous g-C_3N_4 with tunable surfacearea. Phys. Chem. Chem. Phys. **15**, 4510–4517 (2013)
25. Z. Jin, N. Murakami, T. Tsubota, T. Ohno, Complete oxidation of acetaldehyde over a composite photocatalyst of graphitic carbon nitride and tungsten(VI) oxide under visible-light irradiation. Appl. Catal. B Environ. **150–151**, 479–485 (2014)
26. X. Dai, M. Xie, S. Meng, X. Fu, S. Chen, Coupled systems for selective oxidation of aromatic alcohols to aldehydes and reduction of nitrobenzene into aniline using CdS/g-C_3N_4 photocatalyst under visible light irradiation. Appl. Catal. B Environ. **158–159**, 382–390 (2014)
27. M. Sumathi, A. Prakasam, P.M. Anbarasan, Fabrication of hexagonal disc shaped nanoparticles g-C_3N_4/NiO heterostructured nanocomposites for efficient visible light photocatalytic performance. J. Cluster Sci. **30**, 757–766 (2019)
28. M. Sumathi, A. Prakasam, P.M. Anbarasan, Microwave induced novel g-C_3N_4/α-Fe_2O_3 hybrid photocatalyst with superior photocatalytic activity and desirable cycling performance. J. Mater. Sci. Mater. Electron. **30**, 3294–3304 (2019)
29. M.S. Hassan, T. Amna, S.S. Al-Deyab, H.-C. Kim, M.-S. Khil, Monodispersed 3D $MnWO_4$-TiO_2 composite nano flowers

Author's personal copy

photocatalysts for environmental remediation. Curr. Appl. Phys. **15**, 753–758 (2015)
30. S. Saranya, S.T. Senthilkumar, K. Vijaya Sankar, R. Kalai Selvan, Synthesis of $MnWO_4$ nanorods and its electrical and electrochemical properties. J. Electroceram. **28**, 220–225 (2012)
31. N. Aloysius Sabu, K.P. Priyanka, X. Sheena, E.M. Mohammed, T. Varghese, in *Enhancement of electrical properties of manganese tungstate nanoparticles by beam irradiation*. IOP Conf. Series: Materials Science and Engineering, vol. 73 (2015), p. 012051
32. X. Yan, K. Liu, W. Shi, Facile synthesis of CdS/$MnWO_4$ heterojunction with enhanced visible-light-driven photocatalytic activity and mechanism investigation. Colloids Surf. A Physicochem. Eng. Asp. **520**, 138–145 (2017)
33. V.R. Raja, A. Karthika, A. Suganthi, M. Rajarajan, Facile synthesis of $MnWO_4$/BiOI nanocomposites and their efficient photocatalytic and photo electrochemical activities under the visible light irradiation. J. Sci. Adv. Mater. Dev. **3**, 331–341 (2018)
34. S. Prabhu, M. Pudukudy, S. Harish, M. Navaneethan, S. Sohila, K. Murugesan, R. Ramesh, Facile construction of djembe-like ZnO and its composite with g-C_3N_4 as a visible-light-driven heterojunction photocatalyst for the degradation of organic dyes. Mater. Sci. Semiconduct. Process. **106**, 10454 (2020)
35. M. Arami, N.Y. Limaee, N.M. Mahmoodi, N. Salman, Equilibrium and kinetics studies for the adsorption of direct and acid dyes from aqueous solution by soy meal hull. J. Hazard. Mater. **135**, 11–19 (2006)
36. I.K. Konstantinou, T.A. Albanis, TiO_2-assisted photocatalytic degradation of azo dyes in aqueous solution: kinetic and mechanistic investigations: a review. Appl. Catal. B **49**, 1–14 (2014)
37. Y.P. Sun, W. Ha, J. Chen, H.Y. Qi, Y.P. Shi, Advances and applications of graphitic carbon nitride as sorbent in analytical chemistry for sample pretreatment: a review. Trends Anal. Chem. **84**, 12–21 (2016)
38. M. Parthibavarman, K. Vallalperuman, S. Sathishkumar, M. Durairaj, K. Thavamani, A novel microwave synthesis of nanocrystalline SnO_2 and its structural optical and dielectric properties. J. Mater. Sci. Mater. Electron. **25**, 730–735 (2014)
39. M.N. Iliev, M.M. Gospodinov, A.P. Litvinchuk, Raman spectroscopy of $MnWO_4$. Phys. Rev. B. **80**, 212302 (2009)
40. L.H. Hoang, N.T.M. Hien, W.S. Choi, Y.S. Lee, K. Taniguchi, T. Arima, S. Yoon, X.B. Chen, I.-S. Yang, Temperature dependent Raman scattering study of multiferroic MnWO4. J. Raman Spectrosc. **41**, 1005–1010 (2010)
41. T.D. Nguyen, D. Mrabet, T.T.D. Vu, C.T. Dinh, T.O. Do, Biomolecule-assisted route for shape-controlled synthesis of single-crystalline $MnWO_4$ nanoparticles and spontaneous assembly of polypeptide-stabilized mesocrystal microspheres. Cryst. Eng. Commun. **13**, 1450–1460 (2011)
42. L. Huang, H. Xu, Y. Li, H. Li, X. Cheng, J. Xia, Y. Xu, G. Cai, Visible-light-induced WO_3/g-C_3N_4 composites with enhanced photocatalytic activity. Dalton Trans. **42**, 8606–8616 (2013)
43. Y. Sun, L. Chen, Y. Wang, Z. Zhao, P. Li, W. Zhang, Y. Leprince-Wang, H. Jie, Synthesis of MoO_3/WO_3 composite nanostructures for highly sensitive ethanol and acetone detection. J. Mater. Sci. **52**, 1561–1572 (2017)
44. M. Parthibavarman, S. Sathishkumar, S. Prabhakaran, M. Jayashree, R. BoopathiRaja, High visible light-driven photocatalytic activity of large surface area Cu doped SnO_2 nanorods synthesized by novel one-step microwave irradiation method. J. Iran. Chem. Soc. **15**, 2789–2801 (2018)
45. M. Parthibavarman, M. Karthik, P. Sathishkumar, R. Poonguzhali, Rapid synthesis of novel Cr-doped WO_3 nanorods: an efficient electrochemical and photocatalytic performance. J. Iran. Chem. Soc. **15**, 1419–1430 (2018)
46. S.L. Prabavathi, V. Muthuraj, Superior visible light driven photocatalytic degradation of fluoroquinolone drug norfloxacin over novel $NiWO_4$ nanorods anchored on g-C_3N_4 nanosheets. Colloids Surf. A Physicochem. Eng. Asp. **567**, 43–54 (2019)
47. K. Saravanakumar, V. Muthuraj, S. Vadivel, Constructing novel Ag nanoparticles anchored on MnO_2 nanowires as an efficient visible light driven photocatalyst. RSC Adv. **6**, 61357–61366 (2016)

Publisher's Note Springer Nature remains neutral with regard to jurisdictional claims in published maps and institutional affiliations.